Reconstruction of CT Images from Sparse-View Polyenergetic Data Using Total Variation Minimization

T. Humphries and A. Faridani

Abstract—Recent work in CT image reconstruction has seen increasing interest in the use of compressive sensing techniques to reconstruct images from sparse-view projection data, with the goal of reducing radiation dose as well as scan time. Most often these reconstruction approaches exploit sparsity in the gradient of the image using total variation (TV) minimization. Following the existing theoretical results from compressive sensing, these approaches typically assume a linear measurement model, which corresponds to data generated from a monoenergetic X-ray beam. Most clinical CT systems generate X-rays from a polyenergetic spectrum, however, which is inconsistent with a linear system model and produces the well-known beam hardening artifacts. Such artifacts have been observed in some studies on sparse-view CT reconstruction using a linear model.

In this work we incorporate an existing polyenergetic iterative technique known as polyenergetic SART (pSART) into a TV minimization reconstruction algorithm. Using numerical phantom experiments, we demonstrate that this polyenergetic TV minimization algorithm is able to reconstruct images free of both undersampling and beam hardening artifacts from sparse-view, polyenergetic projection data.

I. INTRODUCTION

Techniques for reconstructing CT images from sparse-view data have the potential to reduce radiation dose to the patient and to reduce scan times. Research in the field of compressive sensing [1]–[3] indicates that given a linear model

$$\mathbf{b} = A\mathbf{x}, \tag{1}$$

with $\mathbf{b} \in \mathbb{R}^m$, $\mathbf{x} \in \mathbb{R}^n$, and $A \in \mathbb{R}^{m \times n}$, it is possible in some circumstances to recover $\mathbf{x}$ exactly from $\mathbf{b}$ even in the underdetermined case $m < n$. Theoretical guarantees of recoverability require that the measurement matrix A satisfy some properties (e.g. the restricted isometry property [3]), and that the image $\mathbf{x}$ is sparse in some sense; the sparser the image, the fewer measurements are required to recover it from $\mathbf{b}$. In CT, it may be reasonable to assume that the discrete gradient magnitude of the image is sparse, i.e. that the object being imaged consists of regions of largely homogeneous tissue separated by sharp edges. Although the system matrices encountered in CT imaging do not satisfy the necessary conditions for compressive sensing theory to *guarantee* recoverability from sparse-view data [4], reconstruction approaches based on minimizing the total variation (TV) of the image, a measure of the discrete gradient magnitude, have been empirically successful (e.g. [5]–[9]).

Department of Mathematics, Oregon State University, Corvallis, Oregon

A typical problem formulation is to find

$$\mathbf{x}^* = \arg\min_{\mathbf{x}} \|\mathbf{x}\|_{TV},$$
$$\text{such that } \|A\mathbf{x} - \mathbf{b}\|_2 \leq \epsilon, \text{ and } \mathbf{x}_i \geq 0 \,\forall\, i, \tag{2}$$

where

$$\|\mathbf{x}\|_{TV} = \sum_j \|D_j \mathbf{x}\|_2. \tag{3}$$

Here $\mathbf{x}$ represents the attenuation map of the image, $\mathbf{b}$ is the post-log measured projection data, A is the CT system matrix, and D_j is a discrete approximation to the gradient of the image at the jth pixel. A standard approach to solving (2) consists of an iteration that alternates between improving data fidelity and minimizing the image TV by steepest descent. Since these two objectives compete with one another, some heuristic is required to ensure continual improvement of the data fidelity. Two examples of algorithms taking this approach are adaptive steepest descent projection onto convex sets (ASD-POCS) [5] and improved TV (iTV) [8].

The use of a linear model (1) for reconstruction of CT images assumes that the measurements are generated from a monoenergetic X-ray beam. If the X-ray beam is polyenergetic, as is the case on many clinical systems, the post-log measured data are a nonlinear function of attenuation. Using a linear model to reconstruct polyenergetic data produces images afflicted by beam hardening artifacts, such as cupping and streaking, which can obscure important diagnostic features of the image. This has led to the development of approaches for reconstructing images from polyenergetic data (e.g. [10]–[15]). To date, however, nearly all approaches for reconstructing images from sparse-view data using TV minimization have used a linear model, cf. (2). It was noted in at least one study that images produced using this approach contained noticeable beam hardening artifacts [7].

Recent work in compressive sensing has shown that recovery of sparse signals from undersampled *nonlinear* measurements is also possible under certain conditions [16]. As in the linear case, it is difficult to establish whether these conditions hold for a polyenergetic CT forward model. Nonetheless, in light of the established empirical success of TV minimization for sparse-view CT reconstruction using a linear model, we investigate a polyenergetic sparse-view reconstruction algorithm. In numerical experiments, we show that the algorithm, denoted pSART-iTV, is able to produce images free of both beam hardening and undersampling artifacts.

II. METHODOLOGY

Our algorithm combines two existing iterative algorithms; iTV [8] and polyenergetic SART [15]. The improved TV (iTV) algorithm consists of an alternating iteration that uses the Simultaneous Algebraic Reconstruction Technique (SART) to promote data fidelity, followed by a steepest descent minimization to reduce the image TV. The main feature of iTV is a heuristic that ensures continual improvement of the data fidelity. Specifically, let $\mathbf{x}^{(k)}$ denote the iterative solution to (2) generated by iTV after k iterations. The $(k+1)$th iteration first consists of an iteration of SART, which generates an image denoted by $\mathbf{x}_{SART}^{(k+1)}$. This is followed by one or more iterations of TV minimization, which produce an image denoted $\mathbf{x}_{TV}^{(k+1)}$. We then define the following three quantities:

$$
\epsilon^{(k)} = \left\| A\mathbf{x}^{(k)} - \mathbf{b} \right\|_2^2
$$
$$
\epsilon_{SART}^{(k+1)} = \left\| A\mathbf{x}_{SART}^{(k+1)} - \mathbf{b} \right\|_2^2 \tag{4}
$$
$$
\epsilon_{TV}^{(k+1)} = \left\| A\mathbf{x}_{TV}^{(k+1)} - \mathbf{b} \right\|_2^2 .
$$

One expects that $\epsilon_{SART}^{(k+1)} < \epsilon^{(k)}$ and $\epsilon_{SART}^{(k+1)} < \epsilon_{TV}^{(k+1)}$ since SART improves data fidelity and the TV step worsens it somewhat. To ensure continual improvement of data fidelity, iTV checks the condition

$$
\epsilon_{TV}^{(k+1)} < (1-\omega)\epsilon_{SART}^{(k+1)} + \omega\epsilon^{(k)}, \ \omega \in (0,1) \tag{5}
$$

at the end of the iteration. The parameter ω controls the permissible amount of smoothing due to TV minimization; a value of $\omega = 0$ implies no smoothing, while $\omega = 1$ would allow smoothing to the point of undoing all progress from the SART iteration. If (5) is satisfied after the TV step, $\mathbf{x}_{TV}^{(k+1)}$ is accepted and assigned to $\mathbf{x}^{(k+1)}$. Otherwise, the algorithm sets

$$
\mathbf{x}^{(k+1)} = \lambda\mathbf{x}_{TV}^{(k+1)} + (1-\lambda)\mathbf{x}_{SART}^{(k+1)}, \ \lambda \in (0,1), \tag{6}
$$

where λ is chosen such that

$$
\left\| A\mathbf{x}^{(k+1)} - \mathbf{b} \right\|_2^2 = (1-\omega)\epsilon_{SART}^{(k+1)} + \omega\epsilon^{(k)}. \tag{7}
$$

The new image is a convex combination of $\mathbf{x}_{SART}^{(k+1)}$ and $\mathbf{x}_{TV}^{(k+1)}$ which satisfies the "target" data fidelity given by the right side of the inequality (5). The value of λ can be found analytically by solving a quadratic equation [8].

Polyenergetic SART (pSART) [15] is a recently proposed adaptation of SART which accounts for polyenergetic data. The linear forward projection of the image, $A\mathbf{x}$, is replaced by a nonlinear polyenergetic forward projection, $\mathcal{P} : \mathbb{R}^n \to \mathbb{R}^m$. This operation is given by

$$
\mathcal{P}(\mathbf{x}) = -\ln\left[\sum_h I_h \exp\left(-A\boldsymbol{\mu}(\mathbf{x}, \varepsilon_h) \right) \right], \tag{8}
$$

where I_h is a weighted, discrete approximation to the continuous beam spectrum at energy level ε_h, and $\mathbf{x}$ is the attenuation map at some reference energy, such as 70 keV. The function $\boldsymbol{\mu}(\mathbf{x}, \varepsilon)$ generates an attenuation map of the object at energy ε using linear interpolation between tabulated

---

```
1:  x ← 0, k ← 0
2:  while k < K do
3:      ε^(k) ← ‖𝒫(x) − b‖²₂
4:      for i from 1 to n_s do (pSART)
5:          x ← x − D_{s(i)} A_{s(i)}^T M_{s(i)} [𝒫_{s(i)}(x) − b_{s(i)}]
6:          x ← max(x, 0)
7:      x_pSART ← x
8:      ε_pSART ← ‖𝒫(x_pSART) − b‖²₂
9:      ε^(k+1) ← (1 − ω)ε_pSART + ωε^(k)
10:     for j from 1 to J do (TV minimization)
11:         x ← x − α · ∇(‖x‖_TV)
12:         j ← j + 1
13:     x_TV ← x
14:     ε_TV ← ‖𝒫(x_TV) − b‖²₂
15:     if ε_TV < ε^(k+1) then
16:         x ← x_TV
17:         ε^(k+1) ← ε_TV
18:     else
19:         Use Newton's method to find λ satisfying
                ‖𝒫[(1 − λ)x_pSART + λx_TV] − b‖²₂ = ε^(k+1)
20:         x ← (1 − λ)x_pSART + λx_TV
21:     if (ε^(k) − ε^(k+1)) < Δε_min then (convergence)
22:         break
23:     k ← k + 1
24: return x
```

Fig. 1. Pseudocode of the pSART-iTV algorithm.

---

attenuation curves for base materials such as fat, soft tissue and bone. In particular, if x_j denotes the linear attenuation coefficient (LAC) of pixel j at the reference energy ε_0, then the attenuation coefficient of that pixel at all other energies is computed as

$$
\mu(x_j, \varepsilon) = \frac{[\mu_{k+1}(\varepsilon_0) - x_j]\mu_k(\varepsilon) + [x_j - \mu_k(\varepsilon_0)]\mu_{k+1}(\varepsilon)}{\mu_{k+1}(\varepsilon_0) - \mu_k(\varepsilon_0)}, \tag{9}
$$

where $\mu_k(\varepsilon)$ and $\mu_{k+1}(\varepsilon)$ are the tabulated, energy-dependent LAC functions for the two base materials with LAC values adjacent to x_j at the reference energy.

To combine iTV and pSART into a polyenergetic TV minimization reconstruction approach (pSART-iTV), we replace the SART iteration of iTV with an iteration of pSART. All linear forward projection operations are replaced with the polyenergetic projection $\mathcal{P}(\mathbf{x})$. Finally, the use of a polyenergetic forward projection operation means that it is no longer possible to find the value of λ in (7) analytically. The value can be found iteratively using Newton's method, however. The proposed algorithm is described in Fig. 1. The matrices D and M on line 4 are defined as $D = \text{diag}\left\{ 1 \Big/ \sum_{k=1}^m |a_{kj}|, j = 1 \ldots n \right\}$, $M = \text{diag}\left\{ 1 \Big/ \sum_{k=1}^n |a_{ik}|, i = 1 \ldots m \right\}$, as in SART. Convergence of pSART was accelerated using an ordered subsets approach, where $s(i)$ denotes the ith subset of the projection data.

III. Numerical experiments

We test the effectiveness of the pSART-iTV method using the the FORBILD head phantom [17]. This phantom simulates a 2D slice through the head, and includes an option to include an "ear insert" on the right side of the phantom. The ear insert produces a phantom whose gradient is less sparse, and also creates more severe beam hardening artifacts. We used a phantom size of 800×800 pixels with a pixel width of 0.375 mm. Two types of data were generated: "exact" data, which were produced using the same forward model $\mathcal{P}$ as pSART-iTV (i.e. the inverse crime), and "inconsistent" data, which included noise and other sources of inconsistency due to model mismatch. While the "exact" data is obviously not realistic, it is useful for determining the undersampling potential of pSART-iTV under ideal circumstances.

In addition to pSART-iTV, a second approach to correct for both beam hardening and undersampling was also investigated. This approach consists of applying a well-known classical technique for beam hardening correction proposed by Joseph and Spital [11], followed by TV minimization applied as a post-processing step. The goal of the comparison was to evaluate whether this less computationally intensive, "smoothed JS" approach is competitive with pSART-iTV. Images were reconstructed from 1440, 720, 360, 288 and 144 equally spaced views over $180°$. iTV and pSART-iTV were run for a total of 25 iterations, with an ω value of 0.5. All images were reconstructed at a reference energy of 70 keV.

Fig. 2 shows reconstructions obtained for the phantom with no ear using 288 views. The FBP and monoenergetic iTV images (left column) suffer from artifacts which obscure low-contrast features near the edge of the skull. In contrast, the pSART-iTV image using exact data (top center) is almost entirely free of undersampling and beam hardening artifacts. The image produced using inconsistent data (bottom center) is somewhat degraded due to the noise and model mismatch, but the important features are still discernible.

Images produced using the smoothed JS approach (right column) are free of severe beam hardening artifacts, but are streakier and noisier than the images produced using pSART-iTV, particularly for the case of inconsistent data. When applying TV minimization as a post-processing step, it is difficult to balance the trade-off of smoothing the undersampling artifacts while also preserving image contrast. In contrast, a strength of the pSART-iTV method is the integration of TV minimization within the iterative reconstruction, which allows the amount of smoothing performed at each iteration to be controlled by ω.

Fig. 3 shows equivalent images for the phantom with the right ear insert, using 360 views. The image quality is comparable to that obtained for the phantom with no ear insert, although the severe streaking artifact caused by the ear insert is challenging to remove. With exact data it is nearly eliminated by pSART-iTV after 25 iterations, while in the inconsistent data case, the streak persists to some extent. As before, we note that the images produced using pSART are qualitatively less streaky and noisy than those produced by smoothed JS.

In Figs. 4 and 5, we show reconstructed images of the two phantoms using pSART-iTV as the number of views decreases. Close inspection reveals mild artifacts appearing in both cases at 360 views; at 288 views there are still only mild artifacts for the phantom with no ear insert, while the phantom with the ear insert has a noticeable artifact on the left side. This is consistent with theoretical results indicating that increased sparsity allows reconstruction of an object from fewer views. At a sampling level of 144 views, there are significant artifacts in both images.

IV. Conclusions

In this paper we have demonstrated empirically that existing techniques for reconstruction of linear (monoenergetic) sparse-view data can be adapted to reconstruction of nonlinear (polyenergetic) data. Our proposed pSART-iTV method is effective in removing artifacts due to both undersampling and beam hardening in digital phantom simulations, including cases with inconsistent and noisy data. A comparison with a second approach, based on classical beam hardening correction followed by TV minimization, demonstrates that the fully iterative pSART-iTV approach produces images that are less streaky and noisy.

References

[1] D. L. Donoho. Compressed sensing. *IEEE Trans. Inf. Theory*, 52(4):1289–1306, 2006.

[2] E. J. Candès, J. Romberg, and T. Tao. Robust uncertainty principles: Exact signal reconstruction from highly incomplete frequency information. *IEEE Trans. Inf. Theory*, 52(2):489–509, 2006.

[3] E.J. Candès, J. K. Romberg, and T. Tao. Stable signal recovery from incomplete and inaccurate measurements. *Communications on pure and applied mathematics*, 59(8):1207–1223, 2006.

[4] J. S. Jørgensen and E. Y. Sidky. How little data is enough? phase-diagram analysis of sparsity-regularized X-ray computed tomography. *Phil. Trans. Royal. Soc. A*, 373(2043):20140387, 2015.

[5] E. Y. Sidky and X. Pan. Image reconstruction in circular cone-beam computed tomography by constrained, total-variation minimization. *Phys. Med. Biol.*, 53(17):4777, 2008.

[6] J. Tang, B. E. Nett, and G.-H. Chen. Performance comparison between total variation (TV)-based compressed sensing and statistical iterative reconstruction algorithms. *Phys. Med. Biol.*, 54(19):5781, 2009.

[7] J. Bian et al. Evaluation of sparse-view reconstruction from flat-panel-detector cone-beam CT. *Phys. Med. Biol.*, 55(22):6575, 2010.

[8] L. Ritschl, F. Bergner, C. Fleischmann, and M. Kachelrieß. Improved total variation-based CT image reconstruction applied to clinical data. *Phys. Med. Biol.*, 56(6):1545, 2011.

[9] X. Han et al. Optimization-based reconstruction of sparse images from few-view projections. *Phys. Med. Biol.*, 57(16):5245, 2012.

[10] G. T. Herman. Correction for beam hardening in computed tomography. *Phys. Med. Biol.*, 24(1):81–106, 1979.

[11] P. M. Joseph and R. D. Spital. A method for correcting bone induced artifacts in computed tomography. *Journal of Computer Assisted Tomography*, 2(1):100–108, 1978.

[12] B. De Man et al. An iterative maximum-likelihood polychromatic algorithm for CT. *IEEE Trans. Med. Imag.*, 20(10):999–1008, 2001.

[13] I. A. Elbakri and J. A. Fessler. Statistical image reconstruction for polyenergetic X-ray computed tomography. *IEEE Trans. Med. Imag.*, 21(2):89–99, 2002.

[14] G. Van Gompel et al. Iterative correction of beam hardening artifacts in CT. *Med. Phys.*, 38(7):S36–S49, 2011.

[15] Y. Lin and E. Samei. An efficient polyenergetic SART (pSART) reconstruction algorithm for quantitative myocardial CT perfusion. *Med. Phys.*, 41(2):021911–1 – 021911–14, 2014.

[16] T. Blumensath. Compressed sensing with nonlinear observations and related nonlinear optimization problems. *IEEE Trans. Inf. Theory*, 59(6):3466–3474, 2013.

[17] Z. Yu et al. Simulation tools for two-dimensional experiments in X-ray computed tomography using the FORBILD head phantom. *Phys. Med. Biol.*, 57(13):N237–N252, 2012.
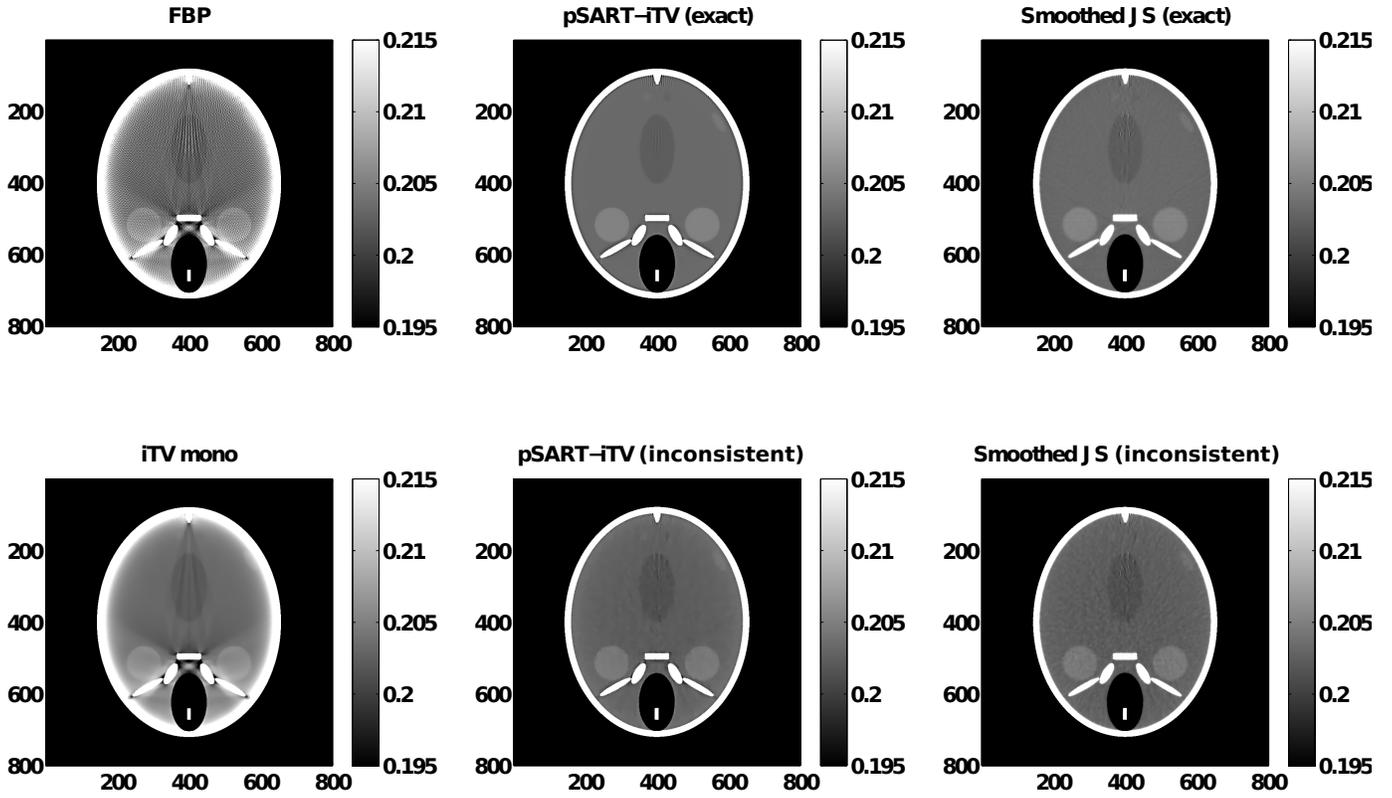
Fig. 2. Images of the phantom with no ear insert produced from 288 view. Top left: image produced from soft tissue corrected FBP. Bottom left: image produced by monoenergetic iTV with soft tissue correction. Top center: image produced using pSART iTV with exact data. Bottom center: image produced using pSART-iTV and inconsistent data. Top right: image produced with the smoothed JS correction and exact data. Bottom right: image produced with the smoothed JS correction and inconsistent data.
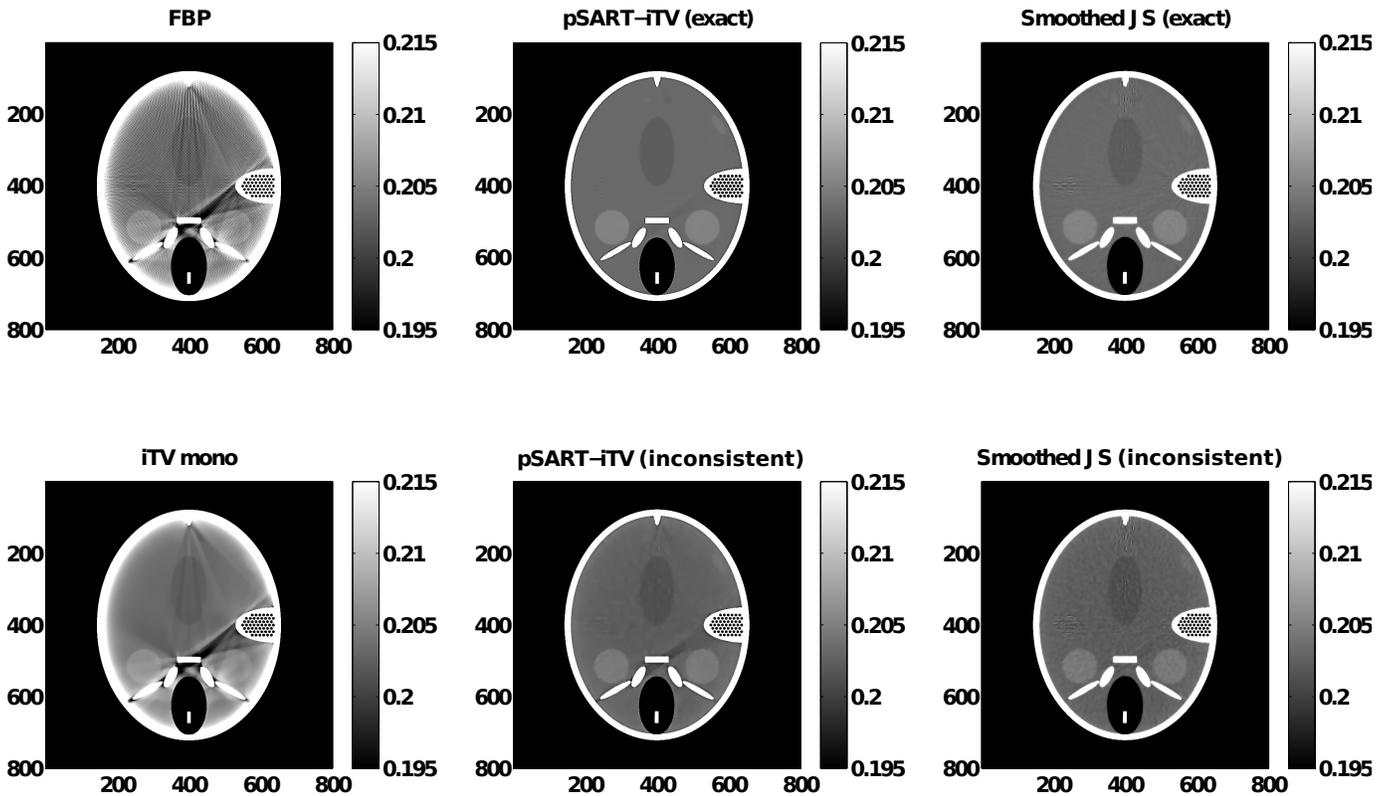
Fig. 3. Images of the phantom with ear insert produced from 360 views. Legend is the same as for Fig. 2.
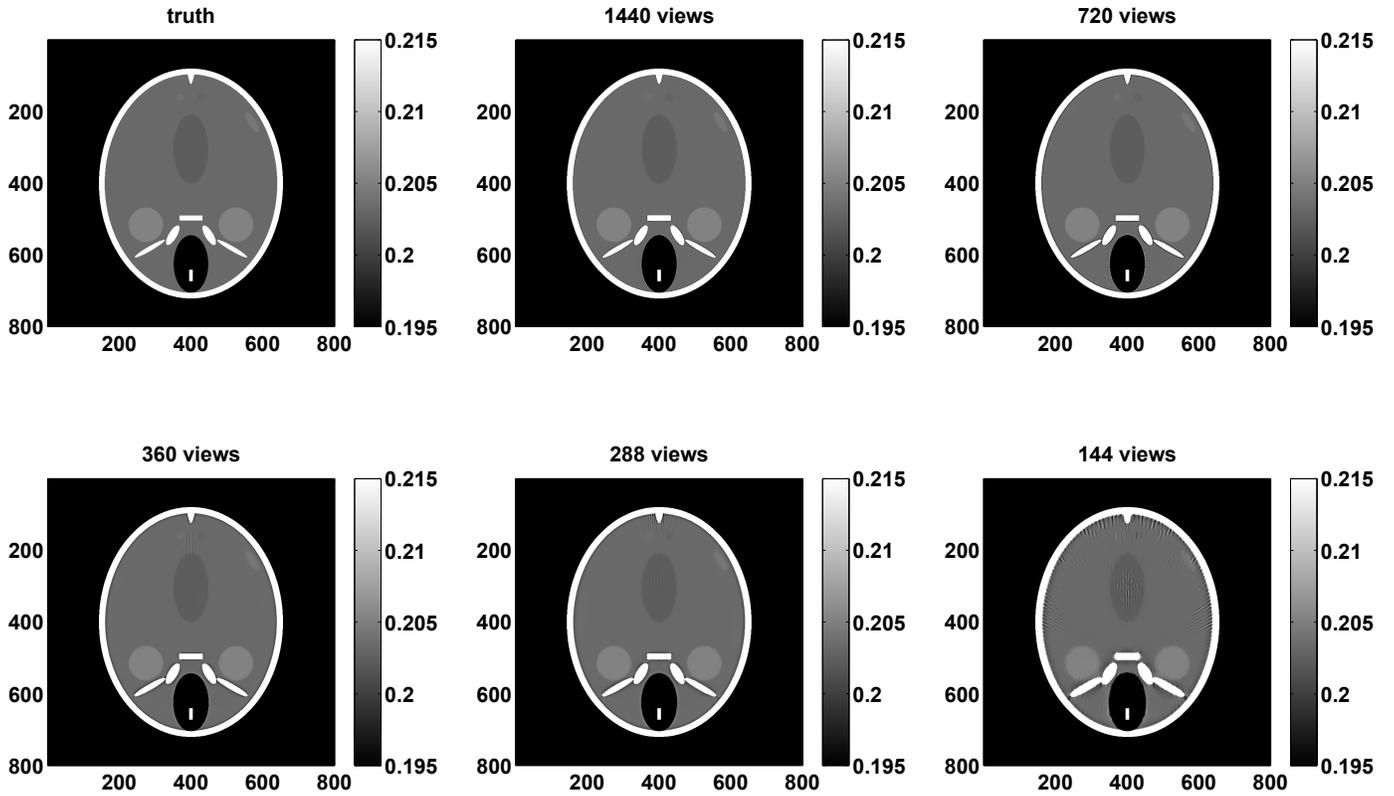
Fig. 4. Images of the phantom with no ear reconstructed with pSART-iTV at different sampling levels. All images reconstructed from the exact data with 25 iterations and $\omega = 0.5$.
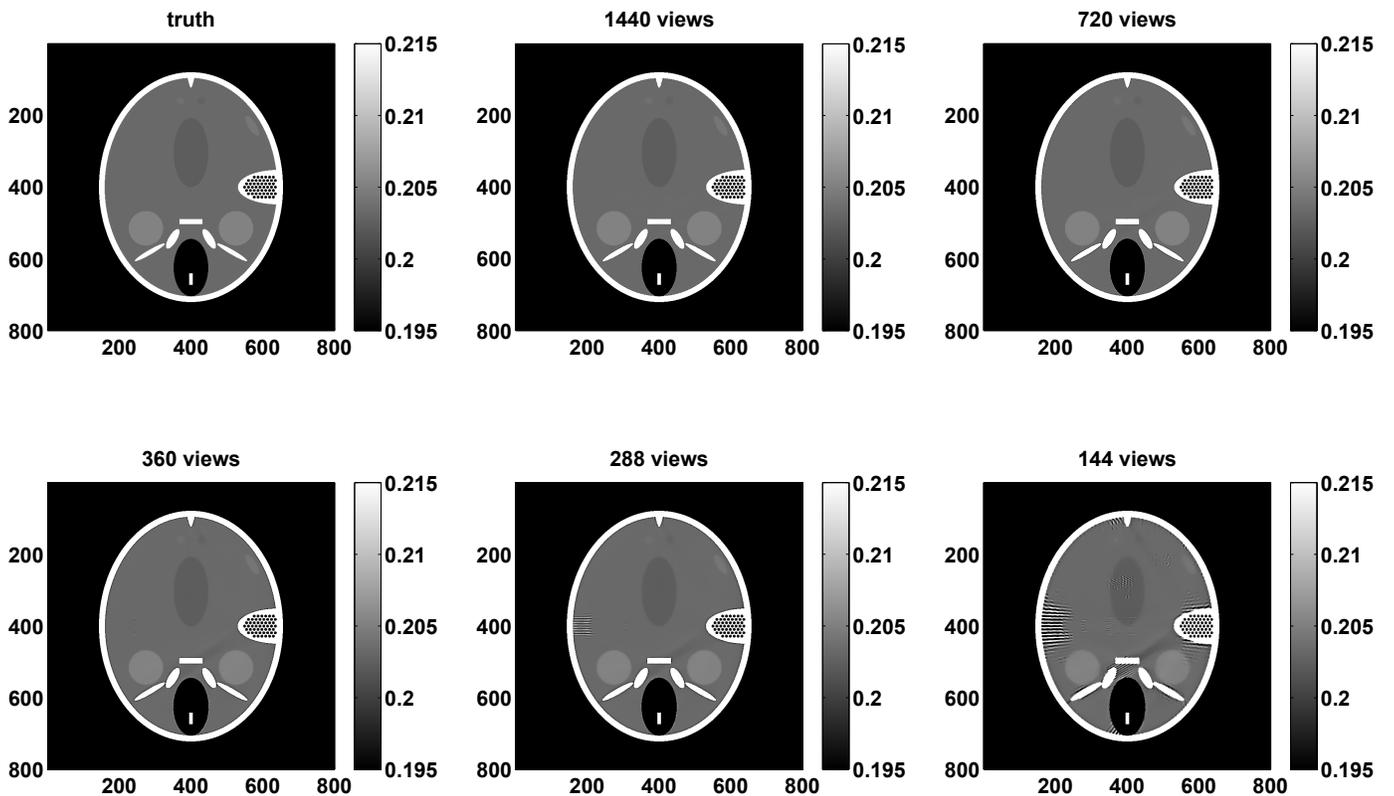
Fig. 5. Images of the phantom with ear insert reconstructed with pSART-iTV at different sampling levels. Parameters are the same as in Fig. 4